

Performance study of the JadePix-3 telescope from a beam test

Sheng Dong^a, Zhiliang Chen^{b,c}, Jia Zhou^{d,a}, Xinye Zhai^{e,a}, Anqi Wang^d,
Yunxiang Wang^d, Hulin Wang^f, Lailin Xu^{b,c}, Jing Dong^a, Yang Zhou^a,
Yunpeng Lu^{a,*}, Mingyi Dong^{a,d}, Hongyu Zhang^{a,d}, Qun Ouyang^{a,d,*}

^a*State Key Laboratory of Particle Detection and Electronics, Institute of High Energy Physics, Chinese Academy of Sciences, BeiJing, 100049, BeiJing, China*

^b*State Key Laboratory of Particle Detection and Electronics, University of Science and Technology of China, Hefei, 230026, Anhui, China*

^c*Department of Modern Physics, University of Science and Technology of China, Hefei, 230026, Anhui, China*

^d*University of Chinese Academy of Sciences, Beijing, 100049, Beijing, China*

^e*Jilin University, Changchun, 130012, Jilin, China*

^f*PLAC, Key Laboratory of Quark & Lepton Physics (MOE), Central China Normal University, Wuhan, 430079, Hubei, China*

Abstract

We present the results of a beam test conducted on a telescope utilizing the JadePix-3 pixel sensor, which was developed with TowerJazz 180 nm CMOS imaging technology. The telescope is composed of five planes, each equipped with a JadePix-3 sensor with pitches of $26 \times 16 \mu\text{m}^2$ and $23.11 \times 16 \mu\text{m}^2$. Additionally, it features an FPGA-based synchronous readout system. The telescope underwent testing using an electron beam with energy ranging from 4 GeV to 6 GeV. At the electron energy of 5.4 GeV, the telescope demonstrated a superior spatial resolution of $2.6 \mu\text{m}$ and $2.3 \mu\text{m}$ in two dimensions, respectively. By designating one plane as the device under test, we evaluated the JadePix-3 sensor's spatial resolution of $5.2 \mu\text{m}$ and $4.6 \mu\text{m}$ in two dimensions, achieving a detection efficiency of over 99.0 %.

Keywords:

Beam telescope, CMOS pixel sensor, Vertex detector, Spatial resolution

*Corresponding author

Email addresses: yplu@ihep.ac.cn (Yunpeng Lu), ouyq@ihep.ac.cn (Qun Ouyang)

1. Introduction

The Circular Electron-Positron Collider (CEPC), proposed by the Chinese particle physics community, is designed to investigate the Higgs boson and conduct essential tests of the fundamental principles underlying the Standard Model, potentially revealing new physics. As a prospective experimental configuration, it imposes stringent technical demands on a variety of detectors. Specifically, the vertex detector necessitates that a single-point resolution of the first layer must be better than $3\mu\text{m}$, and the power consumption of the sensors and readout electronics should not exceed $50\text{ mW}/\text{cm}^2$ [1, 2].

The JadePix-3 pixel sensor is a prototype design for the CEPC vertex detector, emphasizing high spatial resolution and low power consumption [?]. It incorporates various analog front-end circuit and digital circuit designs, and its pixel matrix is divided into four distinct sectors. Each sector comprises 512 rows and 48 columns of pixels. The pixel pitch measures $26.0 \times 16.0\ \mu\text{m}^2$ for sectors 0, 1, and 3, and $23.11 \times 16.0\ \mu\text{m}^2$ for sector 2. Figure 1 depicts the sensor's layout, featuring a sensor size of $6.1 \times 10.4\ \text{mm}^2$ and a pixel matrix area of $4.85 \times 8.19\ \text{mm}^2$.

The sensor's functions and performance have undergone extensive laboratory testing. Key parameters, such as the minimal threshold, power consumption, noise hit rate, and position resolution, have been thoroughly characterized[3]. An infra-red laser beam test system was utilized to assess the single-point position resolution[4], revealing that the resolution falls within the range of $pitch/2\sqrt{12}$ and $pitch/\sqrt{12}$. With the sensor's small pitch, particularly in the row direction, there is potential to construct a high-resolution beam telescope using this sensor. Our objective is to develop a high-precision measurement tool for testing the JadePix-3 itself and the subsequent series of chips.

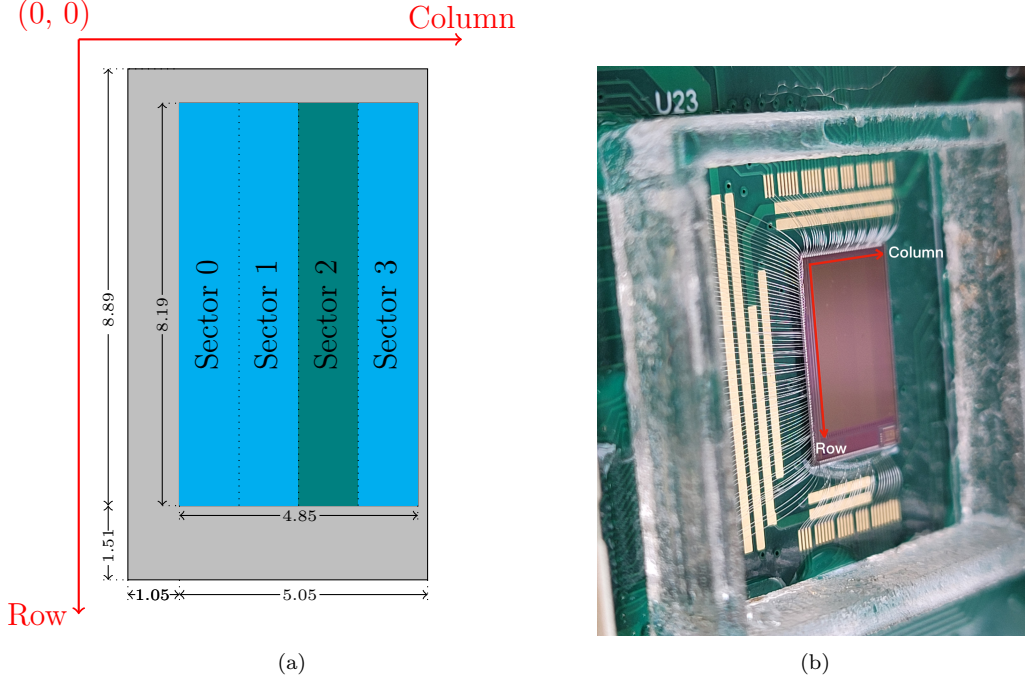


Figure 1: (a) The JadePix-3 layout. The gray area illustrates the pixel periphery, while the cyan and teal area represents the pixel array. Sectors 0, 1, and 3 feature a pitch of $26 \times 16.0 \mu\text{m}^2$, whereas sector 2 has a pixel pitch of $23.11 \times 16.0 \mu\text{m}^2$. Each sector's pixel matrix comprises 48 columns and 512 rows. (b) A photograph of a wire-bonded chip.

2. The JadePix-3 telescope implementation

2.1. Telescope setup

As depicted in Figure 2, the JadePix-3 telescope comprises five planes labeled as P0, P1, P2, P3, and P4, with P2 being the Device Under Test (DUT). The distance between the planes is fixed to 26 mm. In Figure 3, a compact and portable frame made of magnesium-aluminum metal is employed to support and protect the telescope. Each telescope plane includes a commercial FPGA evaluation board, KC705, a sensor bonding board, and an FMC adaptor facilitating communication between the sensor and the FPGA. The FPGA board is utilized for configuring the parameters of the sensor, controlling its readout process, and transmitting the sensor data to the PC via Ethernet.

The global coordinate system is established as a right-handed Cartesian system, with the positive z-axis aligned with the beam direction, and the

origin defined within the plane P2.

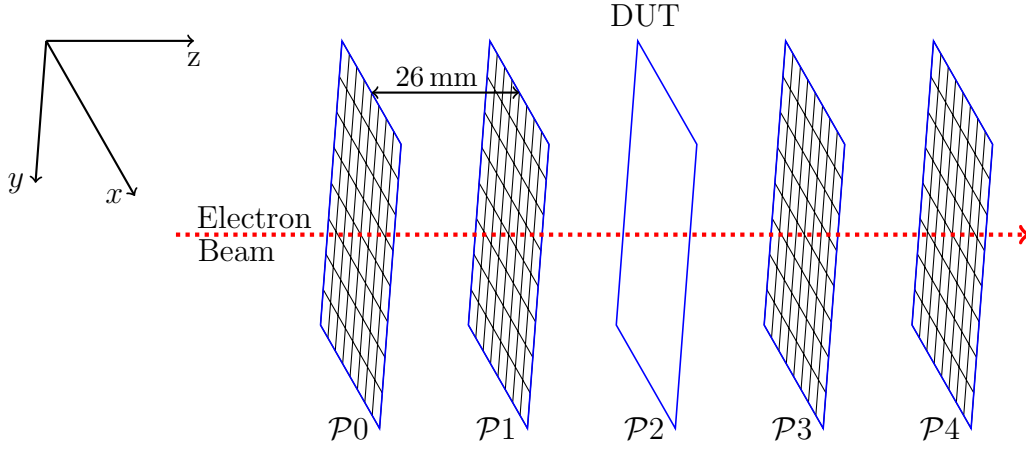


Figure 2: The JadePix-3 telescope is composed of five parallel planes, each spaced 26 mm apart. P0, P1, P3, and P4 serve as reference planes, while P2 is defined as the DUT plane.

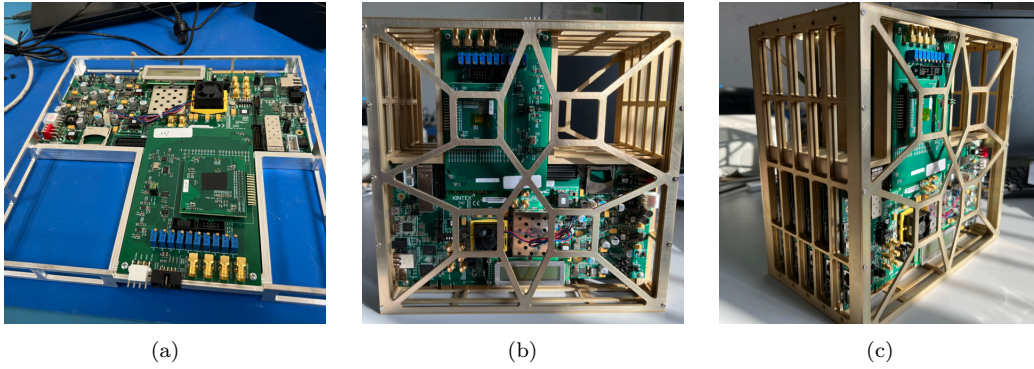


Figure 3: Photographs of the JadePix-3 telescope. (a) Single telescope plane. (b) Front view. (c) Side view.

2.2. Design for synchronous readout of multiple chips

A Data Acquisition (DAQ) system, utilizing the IPbus framework, was developed [5]. The IPbus framework, which employs the User Datagram Protocol (UDP) for network communication, offers excellent scalability [6]. This scalability was a key factor in selecting IPbus, as it facilitated the seamless expansion to a multi-chip readout system.

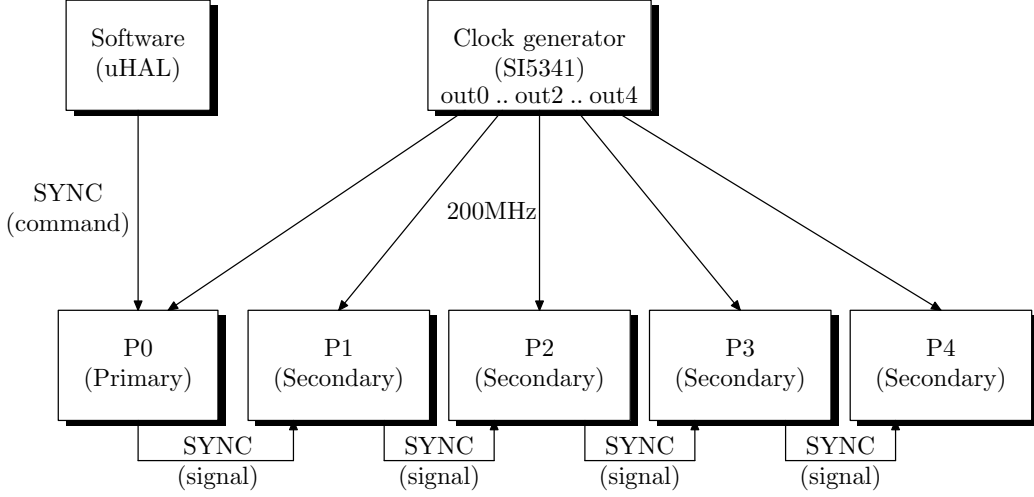


Figure 4: Clock distribution and synchronized start signal link in the readout design. A software command using the IPbus protocol is sent to the primary plane P0, and a SYNC signal is transmitted via a daisy-chain link to the next secondary plane sequentially.

We utilized the SI5341-D-EVB, a commercial clock generator evaluation board, to provide synchronous system clock for each telescope plane, as depicted in Figure 4. This configuration ensures that the telescope planes operate within the same clock domain. To synchronize the start of time in each telescope plane, a daisy-chain signal link was devised. The synchronous start command (SYNC) is initially issued via an end-user Application Program Interface (API) based on the micro Hardware Access Library (uHAL). Upon receiving the SYNC command, the primary plane P0 generates a SYNC signal and sequentially transmits it to the next secondary plane. An external trigger is not necessary since the sensors are read out continuously for all the pixel hits. The delay in the daisy-chain link is less than 100 ns, a duration negligible compared to the sensor’s integration time of 98.3 μ s for each readout frame. This approach guarantees that all planes start operations in a synchronized way.

3. Experimental Set-up

The DESY-II test beam facility provides electron/positron beams with user-selectable momenta ranging from 1 GeV/c to 6 GeV/c, and a divergence of approximately 1 mrad [7]. Beam test data were collected at TB21, one of

the three independent beam lines at the facility. The JadePix-3 telescope was positioned downstream of the beam line, behind the MIMOSA telescope [8] and the TaichuPix telescope [9]. Figure 5 illustrates the experimental set-up. The JadePix-3 telescope shared the beam time and collected data independently.

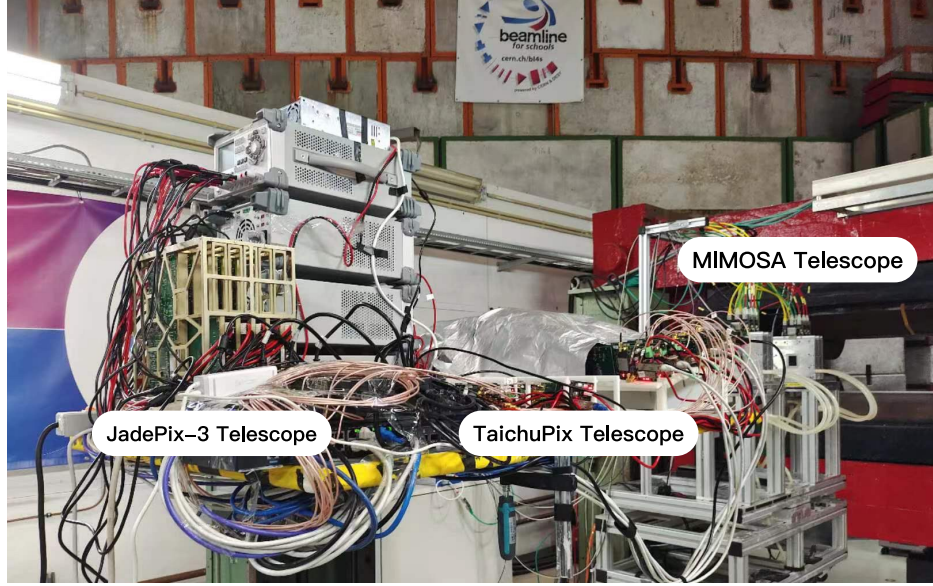


Figure 5: Experimental setup at DESY TB21. The JadePix-3 telescope was positioned downstream of the beam line, following the MIMOSA telescope and the TaichuPix telescope. The JadePix-3 telescope shared the beam time and collected data independently.

4. Data Analysis and Results Discussion

The Corryvreckan framework [10] is used for offline data analysis. The standard procedure for offline analysis involves decoding raw data, clustering, alignment, and track fitting. Subsequently, the performance of the Telescope and DUT is analyzed based on this foundation.

A dedicated event loader module, EventLoaderJadepix3, was developed to import binary hit information from the raw data files of each JadePix-3 sensor. The Metronome module was employed to segment the data stream into regular time frames of a specified length, with the time frame set to 98.316 ps, corresponding to the rolling shutter frame readout time. Standard Corryvreckan modules, including clustering, tracking, and alignment, were

utilized for precise alignment. Two track reconstruction methods were employed: the straight-line and the General Broken Lines (GBL). The GBL served as the primary reconstruction algorithm, considering the effects of multiple scattering and providing more accurate analytical results. The straight-line method was used for analyzing track angles.

To simplify the analysis, data from the left half (sector 0 and sector 1) of the pixel matrix were chosen, while data from the right half (sector 2 and sector 3) were excluded due to the different pitch in sector 2. Consequently, the pixel pitch related to the analytical results corresponds to a size of $26 \times 16 \mu\text{m}^2$.

4.1. Cluster Size Distribution

The Clustering4D module in Corryvreckan conducts the clustering of pixel hits with coinciding timestamps. Given that JadePix-3 sensors provide binary information, the cluster position is determined by utilizing pixel hits with adjacent positions and timestamps.

Figure 6a displays the cluster size (CS) distribution of the DUT with the threshold set to $200 e^-$. The average cluster size is found to be 3.7, with average cluster width and height (projected in x and y directions) measured at 1.6 and 2.4, respectively, as illustrated in Figure 6b. The normalized cluster size distribution, as shown in Figure 6a, shows a gradual decrease for cluster sizes larger than 2. Cluster sizes smaller than 4 account for 76 % of the total number, with those smaller than 8 constituting 93 %.

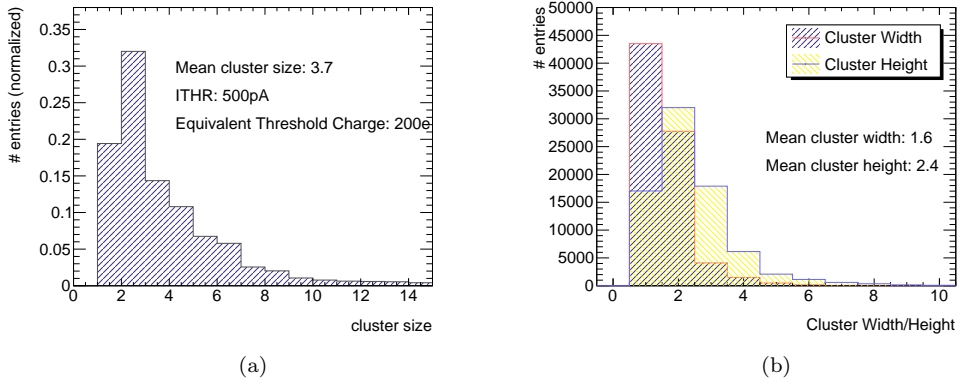


Figure 6: (a) The cluster size distribution of the DUT. (b) The distribution of cluster width and cluster height of the DUT. Experiment parameters: beam energy = 5.8 GeV, threshold = $200 e^-$.

Figure 7 illustrates the intra-pixel track distribution with cluster sizes of 1, 2, 3, and 4 pixels, respectively. When the CS is 1, the particle's incident position is more likely to be at the center of the pixel, as shown in Figure 7a. In contrast, when the hit position is at the four sides of a pixel, multiple pixels are more likely to be fired due to the charge sharing effect. This effect is especially pronounced in the middle of the long sides with a CS of 2, as depicted in Figure 7b, and also at the corners with a CS of 4, as shown in Figure 7d. For comparative purposes, this study also references the findings presented in reference [?], which discusses results obtained with a finer pixel pitch of $18.4 \times 18.4 \mu\text{m}^2$.

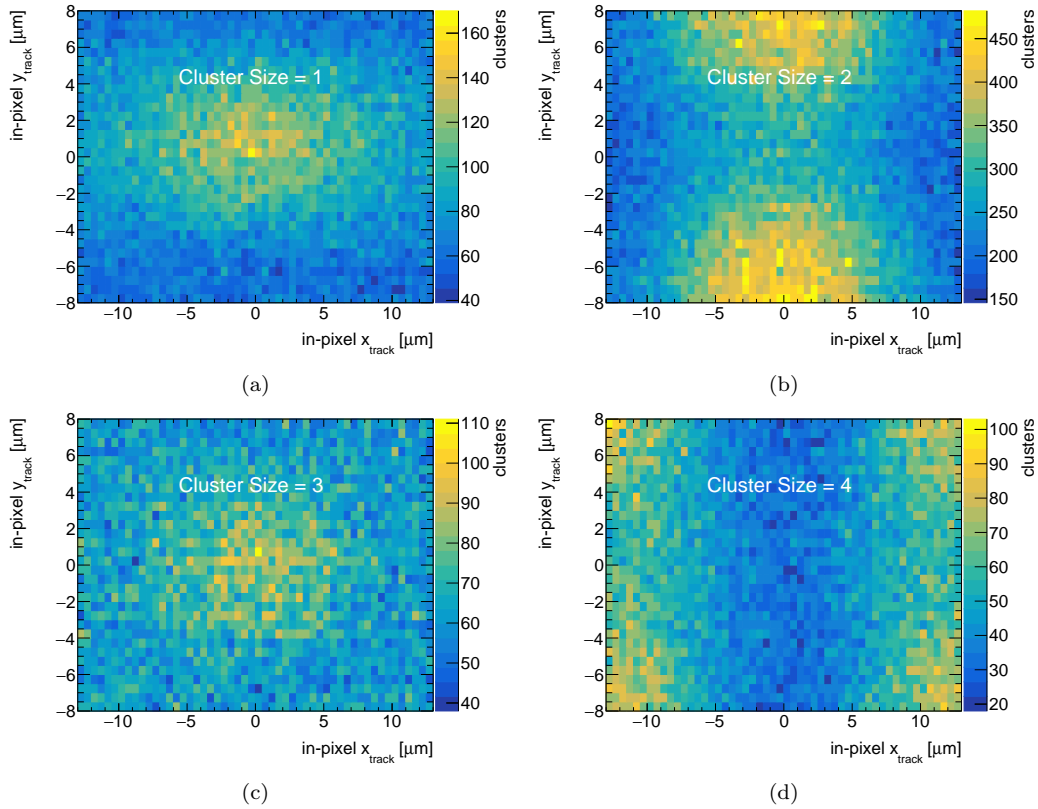


Figure 7: The unbiased intra-pixel track distribution at the DUT for cluster sizes ranging from 1 to 4, respectively. Experiment parameters: beam energy = 5.8 GeV, threshold = $200 e^-$.

To further explore the factors influencing the track distribution for a CS of 3, as demonstrated in Figure 7c, we categorized various cluster patterns

and plotted their intra-pixel track distribution, as depicted in Figure 8. Two distinct categories of patterns were identified: Pattern 1, as shown in Figure 8a, is characterized by three pixels lined consecutively in the y direction. Pattern 2, demonstrated in Figure 8b, features three pixels spanned in both the x and y directions. The occurrence rates for Pattern 1 and Pattern 2 are 53.3 % and 46.3 %, respectively. In Pattern 1, the firing of the central pixel tends to have the pixels immediately above and below it fired as well. For Pattern 2, firing occurs more readily at the short side of pixels, leading to adjacent pixels firing in both x and y directions.

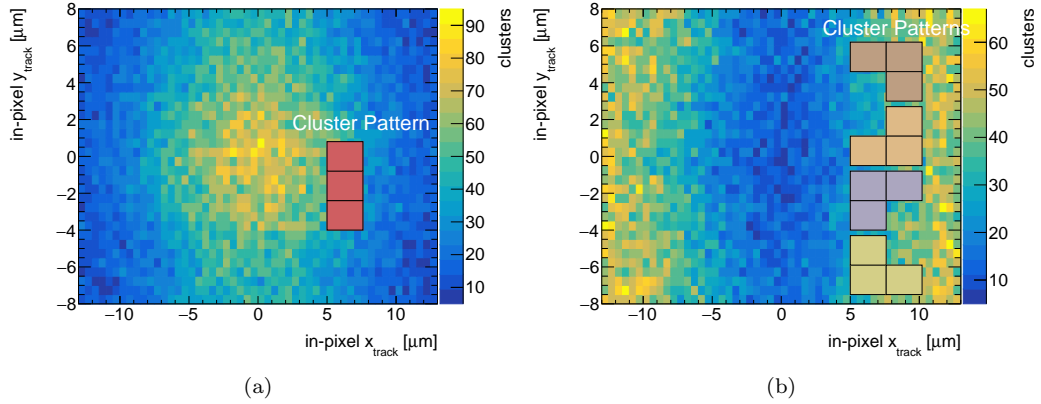


Figure 8: Intra-pixel track distribution for two categories of cluster patterns with $CS = 3$. (a) Cluster Pattern 1 with three pixels lined consecutively in the y direction (b) Cluster Pattern 2 with three pixels spanned in both the x and y directions. Experiment parameters: beam energy = 5.8 GeV, threshold = 200 e^- .

4.2. Alignment and Tracking

According to the guidelines outlined in the Corryvreckan manual [11], the alignment procedure comprises the following steps: 1. Pre-align the telescope planes, 2. Finely align the telescope planes, 3. Pre-align the DUT plane, 4. Finely align the DUT plane. For the telescope alignment, it is specified that each telescope plane must have a cluster concurrently.

The alignment performance can be evaluated by examining the χ^2/n_{dof} (chi-square per degree of freedom) of track fitting and the distance distribution between the track and the hit. Figure 9a displays the χ^2/n_{dof} distribution, with a mean value of 0.96. The notably low mean value indicates a close alignment between the fitted tracks and the cluster positions. Additionally,

Figure 9b illustrates the distribution of distances between the track and hit, revealing minimal distances in both x and y directions, with symmetry about the origin in both directions. These results collectively indicate precise and reliable tracking performance.

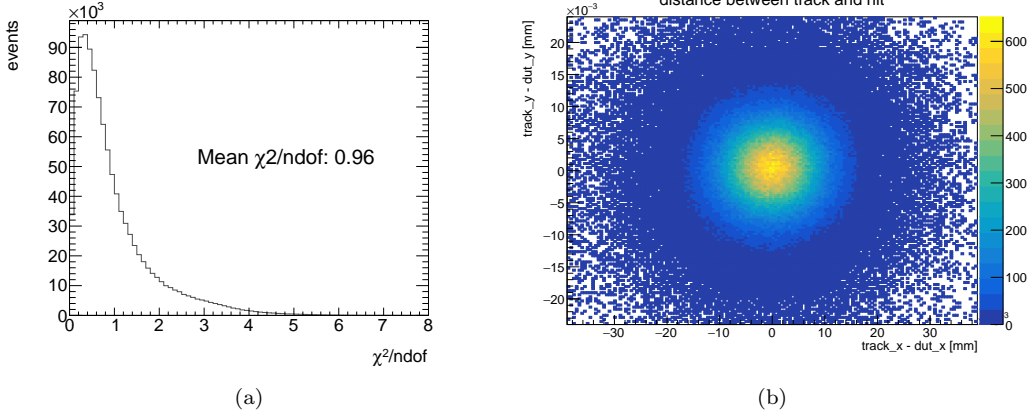


Figure 9: Assessment of alignment performance through (a) the distribution of χ^2/n_{dof} of track fitting and (b) the distribution of the distance between the track and the hit. Experiment parameters: beam energy = 5.8 GeV, threshold = 200 e^- .

4.3. Residual and Spatial Resolution

Utilizing track fitting, hit prediction points corresponding to the DUT measurement points are obtained, enabling the determination of the hit position residual distribution on the DUT. The unbiased residual distributions in the x and y directions are illustrated in Figure 10, where the red/blue line represents the Gaussian fit of the data. The σ of the position residual distribution for the DUT in the x and y directions are 6.7 μm and 5.2 μm , respectively.

In order to precisely determine the spatial resolution of the DUT plane, it is essential to remove the contribution of the telescope system, as described in Equation 1. As indicated in Equation 2, σ_{tel} can be related to σ_{plane} with a scaling factor k [12], assuming that all planes have the same intrinsic resolution, and the reference planes are symmetrically positioned around the DUT at z_0 . The factor k can be calculated using Equation 3, which takes into account the distance between each plane.

$$\sigma_{meas}^2 = \sigma_{DUT}^2 + \sigma_{tel}^2 \quad (1)$$

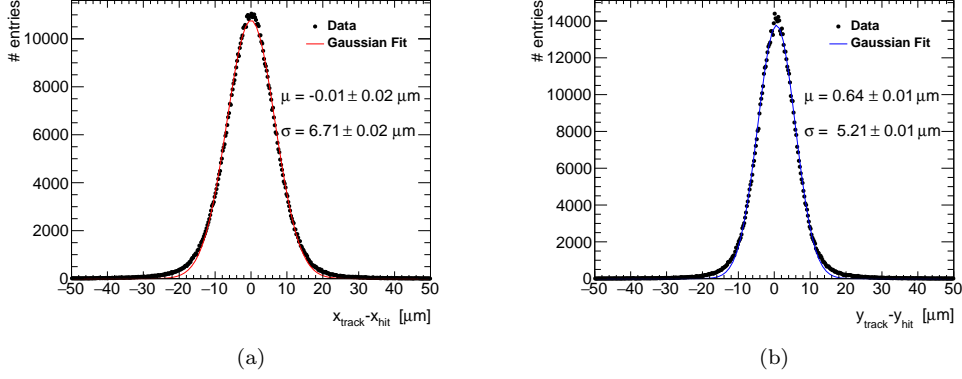


Figure 10: Unbiased residual distribution in (a) the x direction and (b) the y direction, with the data represented by dots and the Gaussian fit shown in red/blue lines. Experiment parameters: beam energy = 5.8 GeV, threshold = 200 e^- .

$$\sigma_{tel}^2 = k\sigma_{plane}^2 \quad (2)$$

$$k = \frac{\sum_i^N z_i^2}{N \sum_i^N z_i^2 - (\sum_i^N z_i)^2} \quad (3)$$

Utilizing Equation 1 and Equation 2, we can deduce Equation 4 and Equation 5.

$$\sigma_{plane}^2 = \frac{\sigma_{meas}^2}{1 + k} \quad (4)$$

$$\sigma_{tel}^2 = \frac{k}{1 + k} \sigma_{meas}^2 \quad (5)$$

The scaling factor k for the JadePix-3 telescope has been calculated as 0.25. Consequently, the spatial resolution for the DUT is determined to be 6.0 μm and 4.7 μm in the x and y directions, respectively. Additionally, the resolution of the telescope is found to be 3.0 μm and 2.3 μm in the x and y directions, respectively.

The unbiased residual distributions in Figure 10 have also been plotted for cluster sizes ranging from 1 to 4 on the DUT. The measured spatial resolutions in the x direction, as depicted in Figure 11, are 9.3 μm , 7.2 μm , 5.7 μm , and 5.3 μm , respectively. Similarly, the results for the y direction are 5.3 μm , 5.5 μm , 5.2 μm , and 4.9 μm , respectively, as presented in Figure 12.

The degraded resolutions can be attributed to the excessive number of tracks outside the favorable regions, as shown in Figure 7. For instance, taking the CS of 1 as an example, the tracks are expected to be concentrated in the center region of the pixel. However, a large portion of tracks hit the peripheral region of pixels, as shown in Figure 7a, leading to the large residual distribution in Figure 11a and Figure 12a.

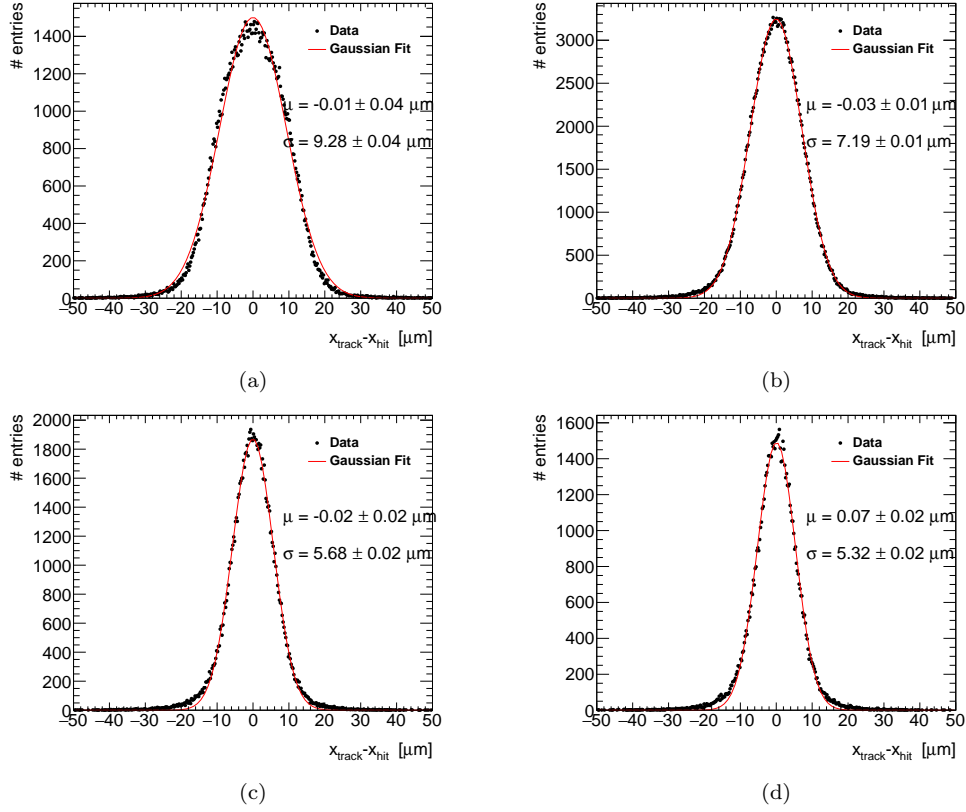


Figure 11: Distribution of residuals in the x direction for different cluster sizes: (a) CS = 1. (b) CS = 2. (c) CS = 3. (d) CS = 4. Experiment parameters: beam energy = 5.8 GeV, threshold = $200 e^-$.

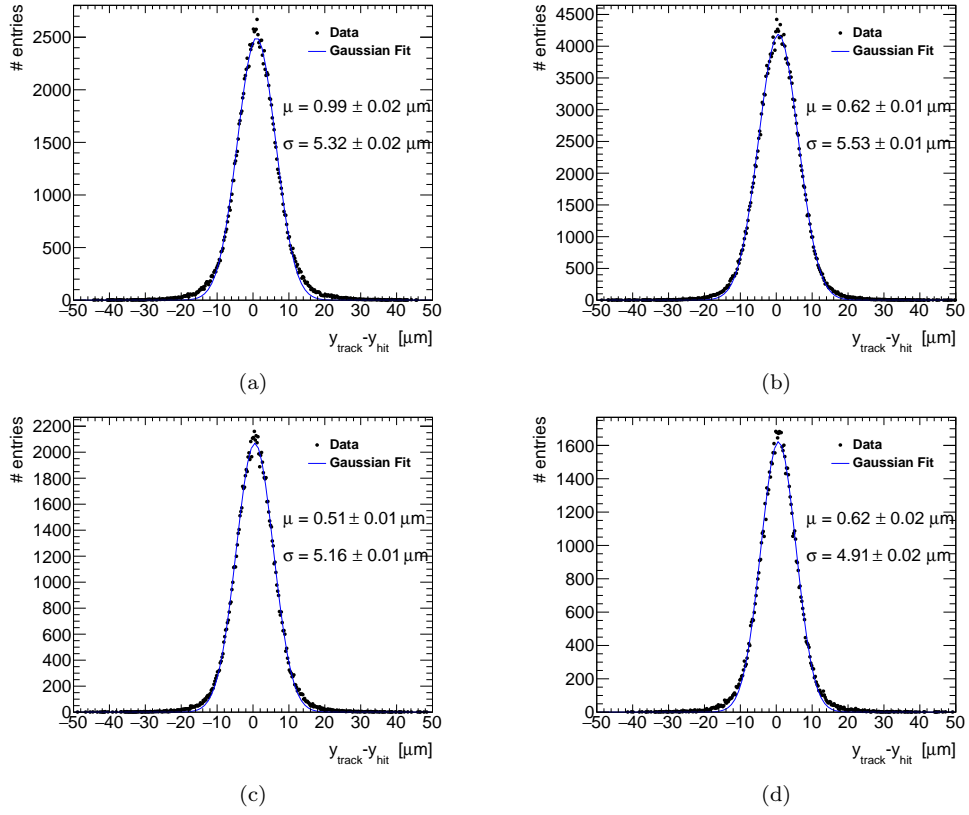


Figure 12: Distribution of residuals in the y direction for different cluster sizes: (a) CS = 1. (b) CS = 2. (c) CS = 3. (d) CS = 4. Experiment parameters: beam energy = 5.8 GeV, threshold = 200 e^- .

4.4. Efficiency

Once all tracks have been reconstructed based on the points from four reference planes, the clusters on the DUT are then associated with the tracks intersecting the DUT. Efficiency is defined as the number of tracks with associated clusters on the DUT over the total number of tracks intersecting the DUT. Figure 13 displays the in-pixel efficiency map, which indicates that the likelihood of a particle being detected by the sensor increases when it strikes at the center of a pixel. The decrease in efficiency at the short sides is still being investigated, but it may be related to the sharing of charge among more pixels if the tracks hit the short sides of pixels, as shown in Figure 7d and Figure 8b.

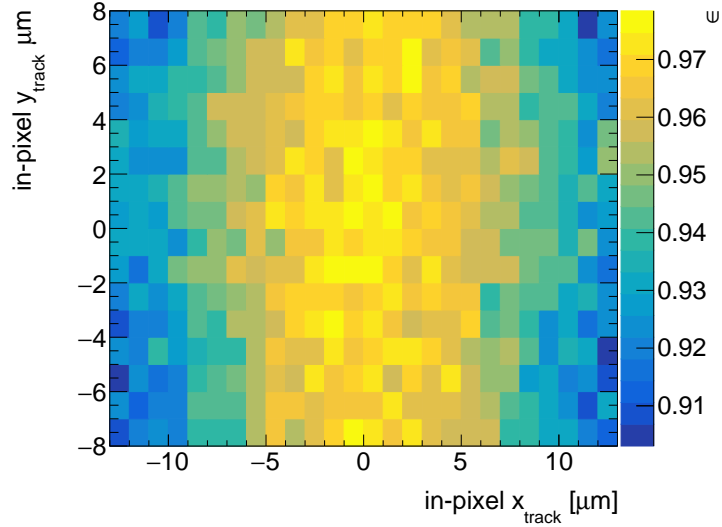


Figure 13: The efficiency plotted as an in-pixel map. Experiment parameters: beam energy = 5.8 GeV, threshold = $200 e^-$. DUT residual cut = $10 * pitch / \sqrt{12}$.

4.5. Threshold Scan

We performed a threshold scan to evaluate changes in several key performance metrics of the sensor, including average cluster size, detection efficiency, and spatial resolution in both x and y directions. As demonstrated in Figure 14a, an increase in the threshold leads to a gradual decrease in the sensor's average cluster size, accompanied by a corresponding reduction in detection efficiency, as shown in Figure 14b. The observed trends are consistent with our expectations. For efficiency and spatial resolution, the DUT

residuals have been confined to a few times of $pitch/\sqrt{12}$ by applying different cut conditions. A larger cut size results in higher detection efficiency, as shown in Figure 14b.

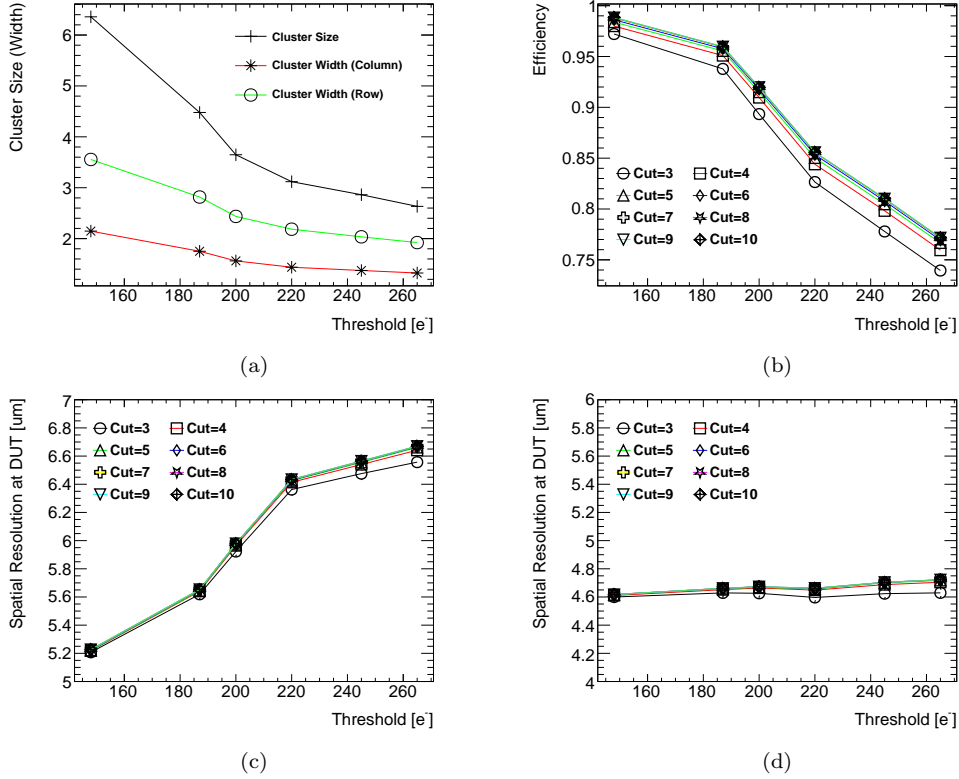


Figure 14: Impact of the threshold scan on (a) Mean cluster size, (b) Efficiency, (c) Resolution in x direction, and (d) Resolution in y direction. The DUT residuals are limited to a few of times of $pitch/\sqrt{12}$ by applying different cut conditions. Experiment parameters: beam energy = 5.4 GeV, threshold range: from 148 e^- to 265 e^- .

In Figure 14c, it is evident that within the threshold scanning range, a higher threshold degrades the spatial resolution in the x direction. While in Figure 14d the spatial resolution in the y direction also degrades, the extent of this degradation is less significant. Reductions of the cut size improve the spatial resolution in both the x and y directions as expected.

According to the findings from the threshold scan, to optimize the detector's performance within this threshold range, a lower threshold is preferable, as it improves both the spatial resolution and the detection efficiency.

5. Conclusion

This study presents the development, testing, and comprehensive analysis of a beam telescope equipped with the JadePix-3 CMOS pixel sensor. The telescope underwent extensive testing at the DESY TB21 facility using an electron beam with energies ranging from 4 GeV to 6 GeV.

An extensive data analysis was performed, including cluster size, detection efficiency, and spatial resolution. At an electron energy of 5.4 GeV, the telescope demonstrated excellent spatial resolution of $2.6\text{ }\mu\text{m}$ and $2.3\text{ }\mu\text{m}$ in two dimensions, respectively. The study also included a comprehensive investigation of various cluster sizes, focusing on the spatial resolution of the JadePix-3 sensor in the DUT plane.

Through the analysis of a series of threshold scanning results, we determined the optimal operational threshold for the sensor. This allowed us to attain the most favorable spatial resolution and efficiency under these specific threshold conditions.

6. Acknowledgements

This study was supported by the National Key Research and Development Program of China (Grant No. 2016YFA0400400) and the Strategic Priority Research Program of the Chinese Academy of Sciences (Grant No. XPB23).

7. Declaration of Generative AI and AI-assisted technologies in the writing process

During the preparation of this work the authors used ChatGPT/OpenAI to rephrase the English wording and expression in formal writing language. After using this tool/service, the authors reviewed and edited the content as needed and take full responsibility for the content of the publication.

References

- [1] C. S. Group, et al., Ceperc conceptual design report: Volume 1-accelerator, arXiv preprint arXiv:1809.00285 (2018).
- [2] C. S. Group, et al., Ceperc conceptual design report: Volume 2-physics & detector, arXiv preprint arXiv:1811.10545 (2018).

- [3] S. Dong, P. Yang, Y. Zhang, Y. Zhou, H. Wang, L. Xiao, L. Zhang, Z. Shi, D. Guo, Z. Wu, et al., Design and characterisation of the jadepix-3 cmos pixel sensor, *Nuclear Instruments and Methods in Physics Research Section A: Accelerators, Spectrometers, Detectors and Associated Equipment* 1048 (2023) 167967.
- [4] Y. Liu, Y. Lu, X. Ju, O.-Y. Qun, Test of a fine pitch soi pixel detector with laser beam, *Chinese Physics C* 40 (1) (2016) 016202.
- [5] S. Dong, Y. Lu, H. Wang, G. Huang, W. Dong, The daq and control system for jadepix3, *Journal of Instrumentation* 16 (07) (2021) P07052.
- [6] C. G. Larrea, K. Harder, D. Newbold, D. Sankey, A. Rose, A. Thea, T. Williams, Ipbu: a flexible ethernet-based control system for xtca hardware, *Journal of instrumentation* 10 (02) (2015) C02019.
- [7] R. Diener, J. Dreyling-Eschweiler, H. Ehrlichmann, I.-M. Gregor, U. Kötz, U. Krämer, N. Meyners, N. Potylitsina-Kube, A. Schütz, P. Schütze, et al., The desy ii test beam facility, *Nuclear Instruments and Methods in Physics Research Section A: Accelerators, Spectrometers, Detectors and Associated Equipment* 922 (2019) 265–286.
- [8] J. Baudot, G. Bertolone, A. Brogna, G. Claus, C. Colledani, Y. Degerli, R. De Masi, A. Dorokhov, G. Doziere, W. Dulinski, et al., First test results of mimosa-26, a fast cmos sensor with integrated zero suppression and digitized output, in: *2009 IEEE Nuclear Science Symposium Conference Record (NSS/MIC)*, IEEE, 2009, pp. 1169–1173.
- [9] T. Wu, S. Li, W. Wang, J. Zhou, Z. Yan, Y. Hu, X. Zhang, Z. Liang, W. Wei, Y. Zhang, et al., Beam test of a 180 nm cmos pixel sensor for the cepc vertex detector, *Nuclear Instruments and Methods in Physics Research Section A: Accelerators, Spectrometers, Detectors and Associated Equipment* 1059 (2024) 168945.
- [10] D. Dannheim, K. Dort, L. Huth, D. Hynds, I. Kremastiotis, J. Kröger, M. Munker, F. Pitters, P. Schütze, S. Spannagel, et al., Corryvreckan: a modular 4d track reconstruction and analysis software for test beam data, *Journal of Instrumentation* 16 (03) (2021) P03008.

- [11] J. Kröger, S. Spannagel, M. Williams, User manual for the corryvreckan test beam data reconstruction framework, version 1.0, arXiv preprint arXiv:1912.00856 (2019).
- [12] A. Bulgheroni, E.-J. Consortium, et al., Results from the eudet telescope with high resolution planes, Nuclear Instruments and Methods in Physics Research Section A: Accelerators, Spectrometers, Detectors and Associated Equipment 623 (1) (2010) 399–401.